Astronomy & Astrophysics

Active galactic nucleus feedback in NGC 3982[*]

P. Joseph[1,2] , K. George[3] , and K. T. Paul[1]

[1] Department of Physics, CHRIST University, Bangalore 560029, India
e-mail: `prajwel.pj@gmail.com`
[2] Indian Institute of Astrophysics, Bangalore 560034, India
[3] Faculty of Physics, Ludwig-Maximilians-Universität, Scheinerstr. 1, Munich 81679, Germany

ABSTRACT

The energetic feedback from supermassive black holes can influence star formation at the centres of galaxies. Observational evidence for active galactic nucleus (AGN) impact on star formation can be searched for in galaxies by combining ultraviolet imaging and optical integral field unit data. The ultraviolet flux directly traces recent star formation, and the integral field unit data can reveal dust attenuation, gas ionisation mechanisms, and gas kinematics from the central regions of the galaxy disk. A pilot study on NGC 3982 shows star formation suppression in the central regions of the galaxy, likely due to negative AGN feedback, and enhanced star formation in the outer regions. The case of NGC 3982 could be observational evidence of AGN feedback operating in a Seyfert galaxy.

Key words. ultraviolet: galaxies – galaxies: individual: NGC 3982 – galaxies: active – galaxies: star formation

1. Introduction

Galaxies in the local Universe host supermassive black holes (SMBHs) with masses $>10^6 M_\odot$ at their centres, which can accrete large amounts of gas from the immediate vicinity (Kormendy & Ho 2013). The accretion changes the SMBH and the host galaxy to an active galactic nucleus (AGN) phase with a net effect of energy release in the form of radiation, jets, and outflows. The energy output can heat the cold molecular gas and increase the turbulence, suppressing star formation and regulating the gas accretion onto the SMBH. This self-regulating process is termed AGN feedback. It is believed to be an important aspect of galaxy formation and evolution, with various pieces of observational evidence supporting it as a star formation quenching pathway for galaxies (see Fabian 2012 and Morganti 2017 for reviews). Active galactic nucleus feedback is included in galaxy simulations to match observed galaxy properties (Springel et al. 2005; Di Matteo et al. 2005; Somerville et al. 2008; Beckmann et al. 2017). While it may be anticipated that this feedback results in the suppression of star formation (negative AGN feedback) due to the copious amount of energy released by the AGN, there is also the inverse case of positive feedback, where star formation is triggered due to AGN activity (Zinn et al. 2013).

Although evidence for AGN feedback is available, direct observations of its influence on star formation in the local Universe remain limited. One reason for the scarcity of direct observations could be that AGN luminosities vary considerably during a typical star-forming episode, and the effect of feedback on star formation may not be readily apparent (Hickox et al. 2014). Such variability can give rise to situations where even if a galaxy's star formation were affected by AGN activity, the corresponding signatures of a strong AGN could have become undetectable. Similarities in star formation efficiencies between Seyfert and inactive local galaxies have been found by Rosario et al. (2018); while this observation may suggest that the AGN activity does not affect star formation efficiencies in AGN host galaxies, it is also possible that the AGN could have been active in the past in inactive galaxies. In studies where the sample of galaxies is selected by AGN activity, it may be challenging to obtain a correlation between the highly variable activity of AGN feedback and star formation that takes place on a relatively long timescale.

However, there may exist galaxies that hosted AGN in the recent past, where we can directly probe the evidence of AGN activity affecting star formation. If we can find such galaxies and study recent star formation in the central regions and its connection to any recent AGN activity, it may lead to a better understanding of the complex relationship of AGN feedback with star formation. Such studies might make it possible to find relatively smoothly time-variable parameters connected to AGN feedback and explore their relationship with star formation as a proxy to unravel how AGN feedback transforms the galaxy.

Among the observations of AGN feedback affecting star formation in nearby galaxies, there are cases of both positive and negative feedback. The AGN jet-induced positive feedback is found in Centaurus A, NGC 1275, and Minkowski's Object (Mould et al. 2000; Canning et al. 2010; Van Breugel et al. 1985). Outflow-induced star formation exists near the nuclear region of NGC 5643 (Cresci et al. 2015). In NGC 7252 and the jellyfish galaxy JO201, AGN activity is proposed to have suppressed star formation in the central region (George et al. 2018, 2019). Both positive and negative feedback has been observed in NGC 5728 (Shin et al. 2019). It will be interesting to increase the statistics of galaxies with evidence of AGN feedback on star formation present in the local Universe.

A comprehensive search for observational signatures of AGN feedback on star formation in nearby galaxies could help unravel the complex spatial and temporal relationship of AGN

---

[*] The 3D animation associated to Fig. 8 is available at `https://www.aanda.org`

interaction with its host galaxy environment. Since AGN are known to impart energy through radiative (sometimes called quasar or wind) and mechanical modes (also known as radio, kinetic, or jet; Harrison 2017), they leave behind observational signatures that could be identified. The gas around AGN will be ionised by the large energy throughput and produce excitation lines that can be spatially mapped. Similarly, star formation can be suppressed or triggered in the galaxy, which can be observed via the absence or presence of emitted ultraviolet (UV) flux associated with star formation activity.

Integral field unit (IFU) based spectroscopy of a galaxy disk allows us to spatially resolve the excitation mechanisms present in the galaxy; this is particularly useful in identifying the extent of AGN-excited regions. The UV imaging data directly probe recent star formation (<200 Myr, Kennicutt & Evans 2012), and any effect of AGN feedback on the galaxy should be revealed in UV images as reduced flux due to suppressed star formation. Integral field unit observations of nearby galaxies from Mapping Nearby Galaxies at APO (MaNGA) and UV data from the Galaxy Evolution Explorer (GALEX) can be used to check for possible spatial evidence of AGN feedback (Martin et al. 2005; Bundy et al. 2014; Gunn et al. 2006; Drory et al. 2015; Smee et al. 2013).

Our objective is to study the impact of AGN activity on star formation using MaNGA and GALEX data. We created a sample of galaxies with the Sloan Digital Sky Survey (SDSS) optical spectral classifications[1] of 'AGN' or 'BROADLINE'. We removed edge-on galaxies from our sample following a visual check of SDSS urz imaging data and selected only those galaxies with both MaNGA and GALEX data. There are 86 galaxies in the sample. NGC 3982 is the nearest face-on galaxy in the sample and was selected for our pilot study, where we demonstrate the feasibility of our project in identifying the effect of AGN activity on star formation. NGC 3982[2] (UGC 6918) is a late-type galaxy at $z = 0.00371$[3]. NGC 3982 is classified as a Seyfert 1.9 type galaxy based on optical spectra (Véron-Cetty & Véron 2010). Very-long-baseline interferometry (VLBI) observations of NGC 3982 in 1.7 and 5 GHz reveal that there could be jet or outflow structures on milliarcsecond scales (Bontempi et al. 2012). González-Delgado & Pérez (1993) noted the presence of circum-nuclear star formation in the galaxy. We note that 1 arcsec in the sky corresponds to 0.076 kpc at a distance of 15.6 Mpc (Wright 2006).

The paper is organised as follows. Section 2 describes the MaNGA, GALEX, and Very Large Array Sky Survey (VLASS) data used for the study and the associated analysis. We discuss the possibility of AGN feedback in NGC 3982 and provide a summary in Sect. 3. We adopt a flat Universe cosmology with $H_o = 71$ km s^{-1} Mpc^{-1}, $\Omega_M = 0.27$, and $\Omega_\Lambda = 0.73$ (Komatsu et al. 2009).

2. Data and analysis

The MaNGA survey observed galaxies up to redshift $z \sim 0.03$. There are 10010 unique galaxies in the final MaNGA data release, DR17 (Accetta et al. 2022). The reduced MaNGA data have a median angular resolution of 2.54 arcsec

---

[1] https://www.sdss.org/dr17/spectro/catalogs/#Objectinformation

[2] http://simbad.u-strasbg.fr/simbad/sim-id?Ident=NGC%203982

[3] http://skyserver.sdss.org/dr17/VisualTools/explore/summary?sid=1146264831163131904

Table 1. General properties of NGC 3982.

Property	Value	References
Redshift (z) [a]	0.00371	Accetta et al. (2022)
Distance [b]	15.6 Mpc	Wright (2006)
Seyfert type	1.9	Véron-Cetty & Véron (2010)
$L_{(2-10\,\mathrm{KeV})}$	10^{40-41} erg s^{-1}	Kammoun et al. (2020)
$L_{(5\,\mathrm{GHz})}$	$\sim 10^{36}$ erg s^{-1}	Bontempi et al. (2012)
Black hole mass	$\sim 10^7\,M_\odot$	Beifiori et al. (2009)

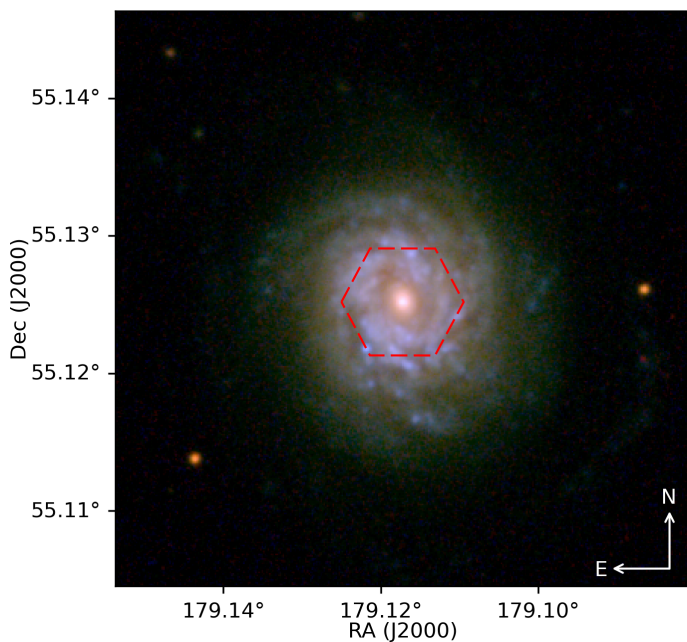**Notes.** [a] From SDSS optical spectra. [b] Derived from z.

Fig. 1. SDSS urz colour image of NGC 3982. The u filter is shown in blue, r is in green, and z is in red. We note the blue regions surrounding the relatively redder nuclear region. The MaNGA IFU hexagonal aperture field of view is overlaid in red.

(Law et al. 2016). A detailed description of the MaNGA sample design can be found in Wake et al. (2017). NGC 3982 was observed with a 127-fibre IFU of 32 arcsec diameter as part of the MaNGA survey (Manga-ID: 1-189584). A summary of a few observed and derived properties of the galaxy is given in Table 1. The SDSS urz colour image cutout of NGC 3982 with the MaNGA IFU hexagonal aperture is shown in Fig. 1.

GALEX was a UV survey mission that had near-ultraviolet (NUV; 5.3 arcsec full width at half maximum) and far-ultraviolet (FUV; 4.2 arcsec full width at half maximum) channels (Morrissey et al. 2007). GALEX observed NGC 3982 in the NUV channel for an effective exposure time of ~2200 seconds (GALEX tile: GI6_012039_HRS74_75). We accessed the NUV imaging data from the Mikulski Archive for Space Telescopes (MAST) GALEX archive (no FUV data were available). The MaNGA resolution corresponds to 0.193 kpc, and the GALEX NUV resolution is 0.403 kpc at the galaxy's distance.

We checked the nature and extent of AGN ionisation in the central region of NGC 3982 as described below. The MaNGA data-analysis pipeline (DAP) generates secondary data products derived from MaNGA spectroscopy (Westfall et al. 2019). The stellar and emission-line kinematics are derived using penalised pixel-fitting (PPXF) software by simultaneously fitting a
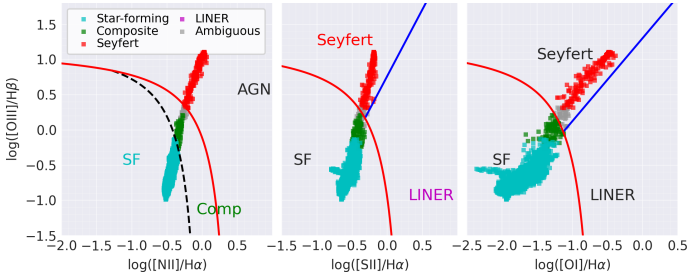
Fig. 2. BPT diagram for NGC 3982 showing [O III]/H$_\beta$ versus [N II]/H$_\alpha$, [O III]/H$_\beta$ versus [S II]/H$_\alpha$, and [O III]/H$_\beta$ versus [O I]/H$_\alpha$ plots. *Left*: MaNGA spaxels classified into star-forming (SF), AGN, composite (AGN + SF), and ambiguous categories. *Middle and right*: MaNGA spaxels categorised as SF, Seyfert, and LINER.

modified MILES stellar library and Gaussian emission-line templates to the MaNGA spectra (the PPXF software employs a maximum penalised likelihood approach to fit templates to spectra; Cappellari 2017; Westfall et al. 2019; Sánchez-Blázquez et al. 2006; Falcón-Barroso et al. 2011). MaNGA DAP products are accessible through `Marvin` software (Cherinka et al. 2019). MaNGA DAP-generated maps of H$_\alpha$, H$_\beta$, [O III] λ5007, [O I] λ6300, [N II] λ6584, and [S II] $\lambda\lambda$6717, 31 emission line intensities were used in our subsequent analysis. To make a spaxel map of the present gas excitation mechanisms, we created a Baldwin-Phillips-Terlevich (BPT) diagram for NGC 3982 using the `get_bpt` function of `Marvin` (Baldwin et al. 1981). `Marvin` uses the classification system of Kewley et al. (2006) and all three diagnostic criteria from [O III]/H$_\beta$ versus [N II]/H$_\alpha$, [O III]/H$_\beta$ versus [S II]/H$_\alpha$, and [O III]/H$_\beta$ versus [O I]/H$_\alpha$ plots. It labels MaNGA spaxels as star-forming (SF), AGN, or composite (AGN + SF). The function marks spaxels as ambiguous when it fails to classify them into one of these three categories. Seyfert galaxy (Seyfert) and low-ionisation narrow emission-line region (LINER) classification is also carried out. A detailed explanation of the function can be found on the `Marvin` documentation website[4]. The generated BPT diagram is shown in Fig. 2, and the on-sky map of spaxel classification in Fig. 3.

We used the GALEX NUV band image to find the spatial distribution of recent star formation. The GALEX NUV image pixel units are in counts per second (CPS), which we converted to flux using the unit conversion factor given in Morrissey et al. (2007):

$$F_{\text{NUV}} = 2.06 \times 10^{-16} \times \text{CPS}, \tag{1}$$

where F_{NUV} is the NUV flux in erg s^{-1} cm^{-2} Å^{-1}. The image in CPS units was subtracted for background before flux conversion. The NUV flux was corrected for Galactic extinction by adopting a Cardelli et al. (1989) law with A_V = 0.0437 (Schlegel et al. 1998) and R_V = 3.1. The dust present in NGC 3982 can attenuate the observed NUV band fluxes, leading to inaccurate interpretation. Therefore, we need to understand the spatial variation of dust attenuation levels, especially in the galaxy's central regions. We used the Balmer decrement, the ratio between two Hα and Hβ emission line flux values, to estimate the dust attenuation. We created the observed Balmer decrement map by calculating the ratio between observed Hα and Hβ emission line maps, (H$_\alpha$/H$_\beta$)$_{\text{obs}}$. Equation (4) from Domínguez et al. (2013) was then
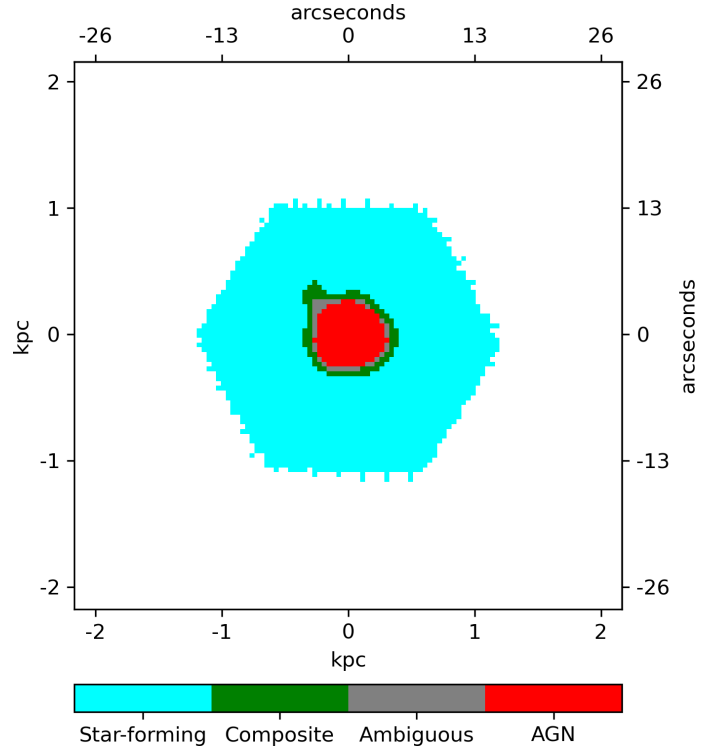
Fig. 3. Spaxel BPT diagram classification of Fig. 2. The figure origin coincides with the galaxy centre. North is up, and east is towards the left. The angular offsets from the origin are given in the top and right axes. The angular offsets have been converted to kiloparsec scales, shown at the bottom and left axes. Star-forming (cyan), composite (green), ambiguous (grey), and AGN (red) categories are shown.

used to convert the Balmer decrement to a colour excess map:

$$E(B - V) = 1.97 \log_{10}\left[\frac{(\text{H}_\alpha/\text{H}_\beta)_{\text{obs}}}{(\text{H}_\alpha/\text{H}_\beta)_{\text{int}}}\right], \tag{2}$$

where $E(B-V)$ is the colour excess map and (H$_\alpha$/H$_\beta$)$_{\text{int}}$ is the expected Balmer decrement map without dust attenuation. We used (H$_\alpha$/H$_\beta$)$_{\text{int}}$ = 3.1 for spaxels falling inside the AGN region of Fig. 3 and 2.86 for the remaining ones (Groves et al. 2012). Finally, we converted the colour excess map to an A_{NUV} map (NUV band attenuation in magnitude) using a Calzetti attenuation law (Calzetti et al. 2000):

$$A_{\text{NUV}} = k_{\text{NUV}} \times E(B-V), \tag{3}$$

where k_{NUV} is the value on the Calzetti reddening curve evaluated at the NUV effective wavelength (2315.7 Å). We find from the A_{NUV} map (see Fig. 4) that the outer and central regions have comparable attenuation levels, with a median A_{NUV} value of 2.04 in the central AGN ionised regions and 2.15 in the galaxy disk.

To correct attenuation by dust in NGC 3982, we used the A_{NUV} map. The extinction- and attenuation-corrected NUV flux was calculated using

$$F_{\text{NUV, corrected}} = F_{\text{NUV}} \times 10^{0.4(A_{\text{NUV, Galactic}} + A_{\text{NUV}})}, \tag{4}$$

where F_{NUV} is the NUV flux, $A_{\text{NUV, Galactic}}$ is the Galactic extinction in the NUV band, and $F_{\text{NUV, corrected}}$ is the extinction- and attenuation-corrected NUV flux. The A_{NUV} map created from the MaNGA data only covers the footprint shown in Fig. 1, which we need to extrapolate to the full galaxy to get the integrated

extinction. Therefore, we used the median value of the A_{NUV} map for the full extent of the NUV image of the galaxy. We note that this estimate should be considered a lower limit; it suggests that the flux could be attenuated by at least a factor of 7.2.

The NUV band luminosity, L_{NUV}, was calculated using

$$L_{\text{NUV}} = 4\pi\, \text{D}^2\, F_{\text{NUV, corrected}}, \tag{5}$$

where D is the distance (see Table 1) and $F_{\text{NUV, corrected}}$ is the attenuation-corrected flux. The NUV band luminosity is in erg s^{-1}. The NUV luminosity was converted to the star formation rate (SFR), assuming constant star formation for 10^8 yr. Equation (4) from Cortese et al. (2008) was used to derive the SFR from L_{NUV}:

$$\text{SFR}\,(M_\odot\,\text{yr}^{-1}) = \frac{L_{\text{NUV}}}{3.83 \times 10^{33}} \times 10^{-9.33}. \tag{6}$$

Figure 5 shows the NUV-derived SFR surface map of the galaxy. A boundary contour encompassing the composite and AGN regions from Fig. 3 is overlaid on the figure. Also shown in the figure is the hexagonal aperture footprint of the MaNGA IFU. The cavity region in the centre matches the composite and AGN photoionised region. We estimated the median SFR density observed in the cavity and the ring-shaped region; there is a factor of ~2 reduction in the SFR density of the cavity region compared to the ring-shaped region.

To check whether the lack of a full disk attenuation map of the galaxy affects our interpretation of the observed cavity region in the centre, we created an azimuthally averaged flux profile of the galaxy using the NUV image as follows. The axis ratio and position angle of NGC 3982 were found on the NASA/IPAC Extragalactic Database (NED) website[5]. Multiple elliptical apertures were defined centred on NGC 3982 with an axis ratio of 0.901 and a position angle of 14.5°, each separated by 1.5 arcsec along the minor axis. The apertures were placed at up to ~0.4 arcmin (2 kpc), and NUV fluxes were estimated. Then the differences between the aperture fluxes were found to get the annuli fluxes. Finally, annuli average fluxes were found by dividing by the annuli area. The annuli average flux is plotted as a function of distance from the galaxy centre in Fig. 6. Similarly, elliptical apertures were used on the A_{NUV} map to estimate the annuli average attenuation levels. These levels were then used to correct the annuli average flux values. Attenuation-corrected annuli average fluxes are also plotted in Fig. 6. We note that the A_{NUV} map only covers the central region of the NUV image. Therefore, we can correct NUV fluxes for attenuation up to ~0.2 arcmin. We stress that attenuation does not affect the NUV profile of the galaxy's central region, as demonstrated in Fig. 6.

We used Very Large Array Sky Survey (VLASS2.1) 2–4 GHz radio sky survey data with an angular resolution of ~2.5 arcsec (Lacy et al. 2020) to probe AGN activity in NGC 3982. We accessed the Quick Look images from the VLASS archive[6]. The VLASS contours are overlaid on the NUV image in Fig. 5. The contours show an elongated structure lying in a south-east to north-west direction. Interestingly, VLBI observations of NGC 3982 in 1.7 and 5 GHz using the European VLBI Network reveal that there could be jet or outflow structures on milliarcsecond scales (Bontempi et al. 2012). The VLBI-detected features are also oriented in a south-east to north-west direction.
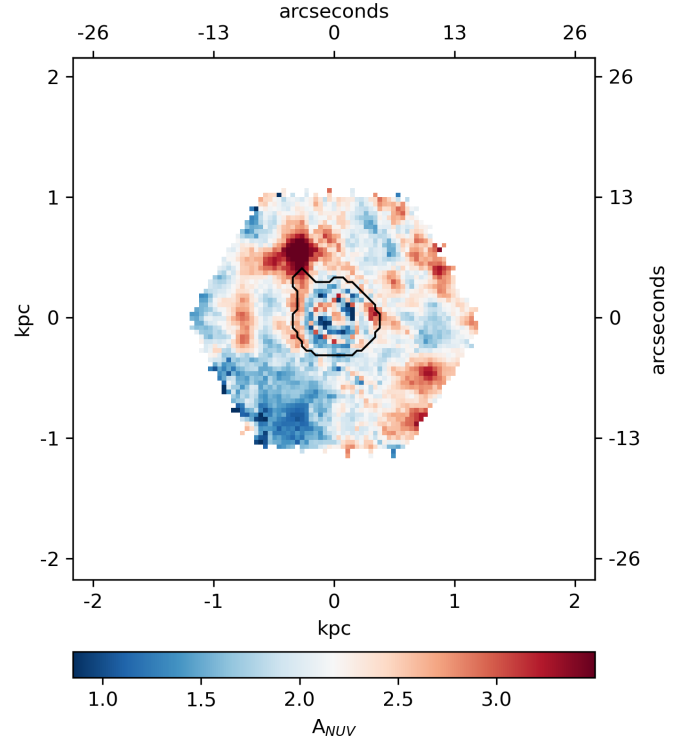

Fig. 4. MaNGA A_{NUV} map of NGC 3982. The black contour represents the area encompassing the composite and AGN regions in Fig. 3.

[O III] is a forbidden optical emission line that is more excited by strong ionising sources, such as AGN, than star-forming regions. Spatially resolved [O III] flux and kinematics maps have been used in AGN feedback studies to trace ionised gas outflows (for example: Shin et al. 2019; Ruschel-Dutra et al. 2021). The [O III] velocity dispersion in AGN host galaxies is mostly due to AGN activity (Rakshit & Woo 2018; Woo et al. 2016). The MaNGA DAP maps of [O III] flux and [O III]-traced ionised gas velocity dispersion are shown in Fig. 7. The velocity dispersion map has been corrected for instrumental dispersion.

3. Discussion and summary

The NUV band directly traces stars formed over the last 200 Myr and, therefore, probes recent star formation (Kennicutt & Evans 2012). The GALEX NUV-derived profile of SFR surface density shows recent star formation in a ring-like region around the centre of NGC 3982 (see Fig. 5). We also created an interactive 3D visualisation[7] of the SFR surface density profile. A snapshot from the interactive plot is shown in Fig. 8. It appears that star formation is suppressed in the central region of NGC 3982.

The intrinsic UV flux from star-forming regions can be modified due to dust attenuation. Even if the central region has the same levels of intrinsic NUV emission as the ring-like region, a large attenuation in the central region can produce the presently observed NUV profile. However, the A_{NUV} map shown in Fig. 4 has comparable dust attenuation levels in the central and outer regions, with a median A_{NUV} value of 2.04 in the central AGN ionised regions and 2.15 in the galaxy disk. We do not see large attenuation levels in the central region. Also, the $F_{\text{NUV, corrected}}$ profile of the galaxy closely matches the F_{NUV} profile (see
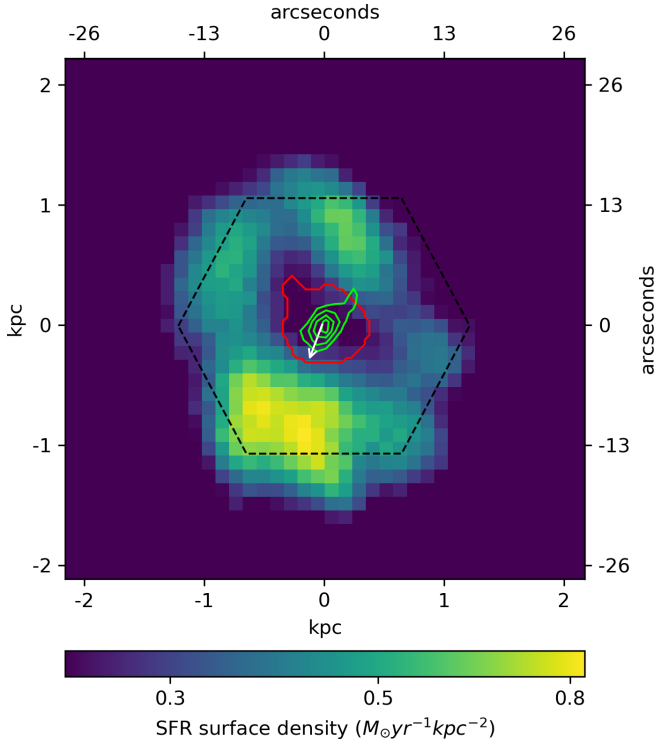

Fig. 5. GALEX NUV image of NGC 3982. The NUV image pixels in count rates have been converted to SFR surface densities in $M_\odot\,\mathrm{yr}^{-1}\,\mathrm{kpc}^{-2}$. The red contour represents the area encompassing the composite and AGN regions in Fig. 3. The dashed black hexagon is the MaNGA IFU field of view. VLASS2.1 radio contours (green) with contour levels 0.0007, 0.0012, 0.0018, and 0.0024 Jy beam^{-1} and a beamwidth of ∼2.5 arcsec are overlaid on the figure. The radio data reveal an elongated structure lying in the south-east to north-west direction. The VLBI-detected jet or outflow direction is shown as a vector (white) for comparison. The vector has an origin at the flat spectrum core profile detected by Bontempi et al. (2012), and it points in the direction of their detected steep spectrum feature.

Fig. 6. Azimuthally averaged NUV flux profile of the galaxy. Both attenuation-corrected and uncorrected flux profiles are shown.

Fig. 6). Therefore, dust attenuation of NUV flux in the galaxy cannot explain the cavity.

The observed suppression of star formation should be a real feature, not an artefact of attenuation. This suggests that processes in the central region prevented star formation in the last 200 Myr. The observed NUV cavity is approximately shaped like an elongated ellipse. We estimate that it has major and minor axis lengths of ∼17 and ∼8 arcsec, respectively (∼1.3/0.6 kpc). The two distinct observational features that require explanation are the ring-like star-forming and star-formation-suppressed central regions.

The first possible explanation we considered is the presence of a bar. Bars are observed to induce star formation along the co-rotation radius and suppress star formation inside it (George et al. 2020). If present, a bar may produce the observed NUV profile in the galaxy. However, Regan & Mulchaey (1999) studied the central region of NGC 3982 using the *Hubble* Space Telescope and ruled out the presence of even a weak bar. NGC 3982 hosts an AGN, and the cavity region is covered by composite and AGN emissions. The boundary contour encompassing the composite and AGN regions overlaid in Fig. 5 shows the extent of AGN ionisation in the galaxy estimated using a BPT diagram. Active galactic nuclei are known to suppress star formation and can also be associated with positive feedback.
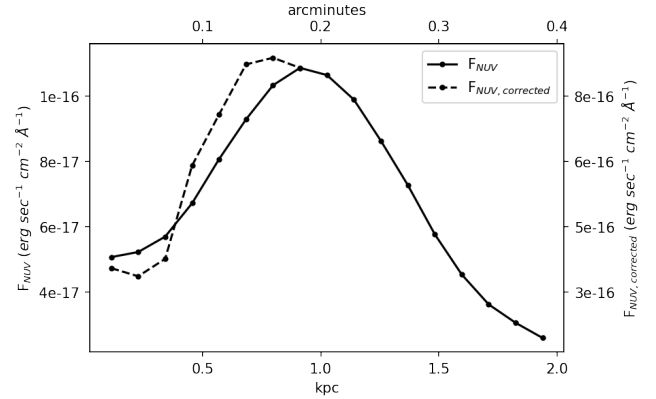
Therefore, the likely mechanism for star formation suppression in NGC 3982 is a jet or outflow associated with the AGN activity.

The radio observations and [O III] flux and velocity dispersion maps provide clues regarding AGN activity. The VLASS2.1 observations reveal an extended structure with elongation in the south-east to north-west direction (see Fig. 5). While the [O III] flux map shows a symmetrically distributed high emission at the central region, the velocity dispersion map shows signs of perturbations in the gas (see Fig. 7). The perturbations are most prominently observed in the south-east (∼130 km s^{-1}) and north-east (∼120 km s^{-1}) regions. The perturbed gas in the south-east is aligned with the elongated VLASS radio structure, and the perturbed gas in the north-east runs parallel to it. These observations clearly show that the ionised gas is perturbed in the AGN-dominated region and that such perturbation may be driven by an AGN jet or outflow. Brum et al. (2017), who analysed the ionised gas kinematics, noted that a mild nuclear outflow could be present in the galaxy. But compared to other local galaxies hosting outflows, ionised gas outflow signatures in NGC 3982 are not prominent (Ruschel-Dutra et al. 2021).

The AGN hosted in NGC 3982 is classified as Seyfert 1.9 and likely belongs to the radiative-mode AGN population. Therefore, the galaxy may have an outflow driven by radiation. We note that the AGN X-ray luminosity is ∼5 orders of magnitude greater than the radio luminosity (see Table 1). Nevertheless, the AGN luminosities in different bands may vary within a short time span (for example, 3C 273; Soldi et al. 2008). A jet may produce outflows with features similar to that generated by radiation (Cielo et al. 2018). Regardless of the nature of the AGN activity, NGC 3982 is perhaps one of the best examples of a nearby low-mass AGN that affects star formation in the disk.

It is interesting to compare the NGC 3982 case with other observations of AGN feedback. Although the activity is presently not detectable, the AGN in NGC 7252 could have been active until recently (Schweizer et al. 2013) and suppressed star formation in the central region of the galaxy (George et al. 2018). In NGC 5728, a star-forming ring with a radius of ∼1 kpc and a cavity is observed, and AGN outflow is found to be responsible (Shin et al. 2019). Surprisingly, ring-like star formation is also observed in NGC 7252 and NGC 3982 at a radius of ∼1 kpc from the centre. While all three galaxies may host a ring-like star-forming region with a radius of ∼1 kpc attributed to AGN feedback, they differ in galaxy morphology and AGN activity.

Based on a multi-wavelength analysis, we present evidence for star formation suppression in the central region of the Seyfert galaxy NGC 3982. As revealed from line diagnostic analysis,
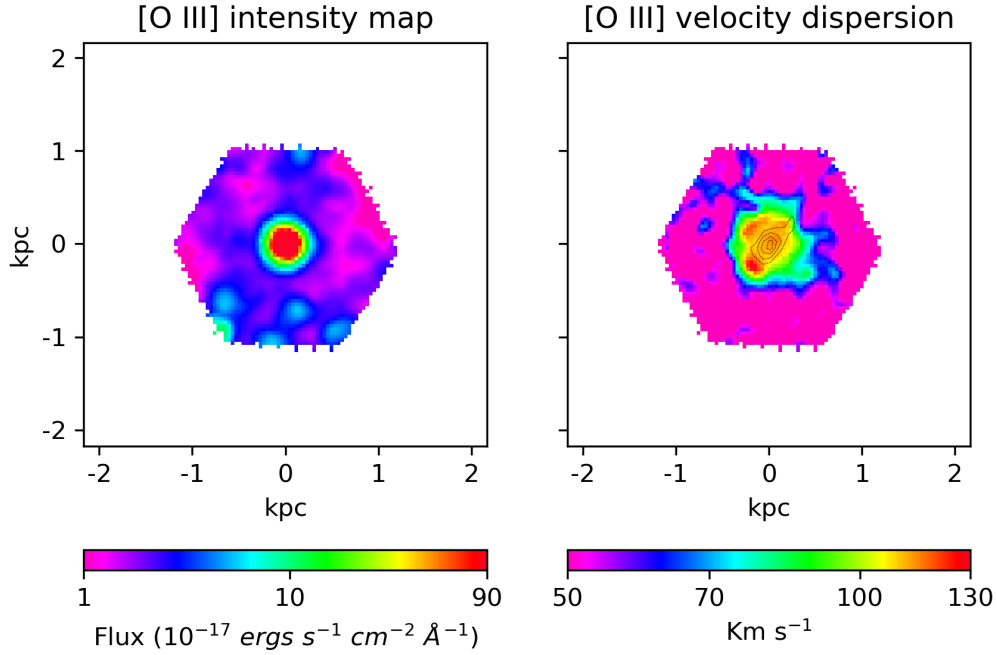
[O III] intensity map [O III] velocity dispersion

Fig. 7. MaNGA derived maps of [O III] emission line intensity and [O III] traced ionised gas velocity dispersion. VLASS2.1 radio contours with contour levels 0.0007, 0.0012, 0.0018, and 0.0024 Jy beam^{-1} and a beamwidth of ~2.5 arcsec are overlaid on the second panel in dashed black lines.
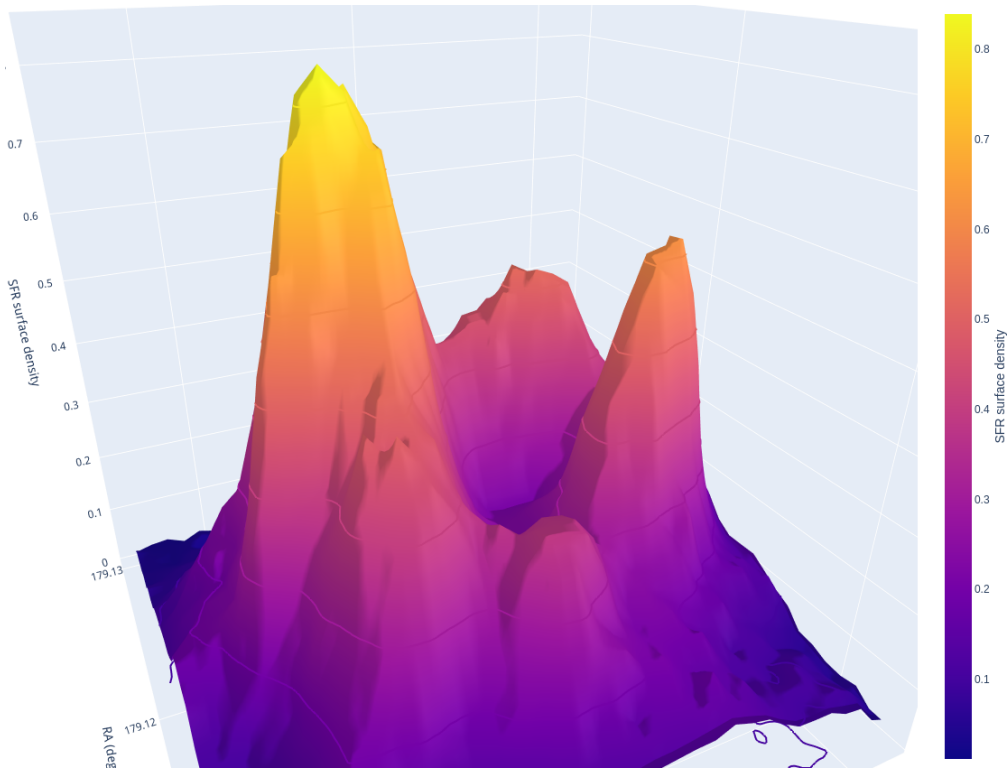

Fig. 8. Snapshot from the interactive 3D animation of the SFR surface density profile of NGC 3982. The visualisation is available online.

the galaxy's central region with reduced star formation is dominated by AGN+composite emission. This is further supported by an AGN jet or outflow revealed from radio and gas velocity dispersion map analysis. The most plausible explanation for the observed scenario presented here is suppression of star formation in the central regions due to feedback from recent AGN activity.

References

Accetta, K., Aerts, C., Aguirre, V. S., et al. 2022, ApJS, 259, 35
Astropy Collaboration (Robitaille, T. P., et al.) 2013, A&A, 558, A33
Astropy Collaboration (Price-Whelan, A. M., et al.) 2018, AJ, 156, 123
Baldwin, J. A., Phillips, M. M., & Terlevich, R. 1981, PASP, 93, 5
Beckmann, R., Devriendt, J., Slyz, A., et al. 2017, MNRAS, 472, 949
Beifiori, A., Sarzi, M., Corsini, E., et al. 2009, ApJ, 692, 856
Bontempi, P., Giroletti, M., Panessa, F., Orienti, M., & Doi, A. 2012, MNRAS, 426, 588
Bradley, L., Sipőcz, B., Robitaille, T., et al. 2022, https://doi.org/10.5281/zenodo.6385735
Brum, C., Riffel, R. A., Storchi-Bergmann, T., et al. 2017, MNRAS, 469, 3405
Bundy, K., Bershady, M. A., Law, D. R., et al. 2014, ApJ, 798, 7
Calzetti, D., Armus, L., Bohlin, R. C., et al. 2000, ApJ, 533, 682
Canning, R., Fabian, A., Johnstone, R., et al. 2010, MNRAS, 405, 115
Cappellari, M. 2017, MNRAS, 466, 798
Cardelli, J. A., Clayton, G. C., & Mathis, J. S. 1989, ApJ, 345, 245
Cherinka, B., Andrews, B. H., Sánchez-Gallego, J., et al. 2019, AJ, 158, 74
Cielo, S., Bieri, R., Volonteri, M., Wagner, A. Y., & Dubois, Y. 2018, MNRAS, 477, 1336
Cortese, L., Gavazzi, G., & Boselli, A. 2008, MNRAS, 390, 1282
Cresci, G., Marconi, A., Zibetti, S., et al. 2015, A&A, 582, A63
Di Matteo, T., Springel, V., & Hernquist, L. 2005, Nature, 433, 604
Domínguez, A., Siana, B., Henry, A., et al. 2013, ApJ, 763, 145
Drory, N., MacDonald, N., Bershady, M., et al. 2015, AJ, 149, 77
Fabian, A. C. 2012, Annu. Rev. Astron. Astrophys., 50, 455
Falcón-Barroso, J., Sánchez-Blázquez, P., Vazdekis, A., et al. 2011, A&A, 532, A95
George, K., Joseph, P., Mondal, C., et al. 2018, A&A, 613, L9
George, K., Poggianti, B. M., Bellhouse, C., et al. 2019, MNRAS, 487, 3102
George, K., Joseph, P., Mondal, C., et al. 2020, A&A, 644, A79
González-Delgado, R. M., & Pérez, E. 1993, Astrophys. Space Sci., 205, 127
Groves, B., Brinchmann, J., & Walcher, C. J. 2012, MNRAS, 419, 1402
Gunn, J. E., Siegmund, W. A., Mannery, E. J., et al. 2006, AJ, 131, 2332
Harris, C. R., Millman, K. J., van der Walt, S. J., et al. 2020, Nature, 585, 357
Harrison, C. 2017, Nat. Astron., 1, 1
Hickox, R. C., Mullaney, J. R., Alexander, D. M., et al. 2014, ApJ, 782, 9
Hunter, J. D. 2007, Comput. Sci. Eng., 9, 90
Inc, P. T. 2015, Collaborative Data Science
Joye, W. A., & Mandel, E. 2003, Astron. Data Anal. Software Syst. XII, 295, 489
Kammoun, E., Miller, J., Koss, M., et al. 2020, ApJ, 901, 161
Kennicutt, R. C., Jr, & Evans, N. J. 2012, Annu. Rev. Astron. Astrophys., 50, 531
Kewley, L. J., Groves, B., Kauffmann, G., & Heckman, T. 2006, MNRAS, 372, 961
Komatsu, E., Dunkley, J., Nolta, M., et al. 2009, ApJS, 180, 330
Kormendy, J., & Ho, L. C. 2013, ARA&A, 51, 511
Lacy, M., Baum, S., Chandler, C., et al. 2020, PASP, 132
Law, D. R., Cherinka, B., Yan, R., et al. 2016, AJ, 152, 83
Martin, D. C., Fanson, J., Schiminovich, D., et al. 2005, ApJ, 619, L1
Morganti, R. 2017, Front. astron. space sci., 4, 42
Morrissey, P., Conrow, T., Barlow, T. A., et al. 2007, ApJS, 173, 682
Mould, J. R., Ridgewell, A., Gallagher, J. S., III, et al. 2000, ApJ, 536, 266
Pérez, F., & Granger, B. E. 2007, Comput. Sci. Eng., 9, 21
Rakshit, S., & Woo, J.-H. 2018, ApJ, 865, 5
Regan, M. W., & Mulchaey, J. S. 1999, AJ, 117, 2676
Robitaille, T., Deil, C., & Ginsburg, A. 2020, Astrophysics Source Code Library [record ascl:2011.023]
Rosario, D., Burtscher, L., Davies, R. I., et al. 2018, MNRAS, 473, 5658
Ruschel-Dutra, D., Storchi-Bergmann, T., Schnorr-Müller, A., et al. 2021, MNRAS, 507, 74
Sánchez-Blázquez, P., Peletier, R., Jiménez-Vicente, J., et al. 2006, MNRAS, 371, 703
Schlegel, D. J., Finkbeiner, D. P., & Davis, M. 1998, ApJ, 500, 525
Schweizer, F., Seitzer, P., Kelson, D. D., Villanueva, E. V., & Walth, G. L. 2013, ApJ, 773, 148
Shin, J., Woo, J.-H., Chung, A., et al. 2019, ApJ, 881, 147
Smee, S. A., Gunn, J. E., Uomoto, A., et al. 2013, AJ, 146, 32
Soldi, S., Türler, M., Paltani, S., et al. 2008, A&A, 486, 411
Somerville, R. S., Hopkins, P. F., Cox, T. J., Robertson, B. E., & Hernquist, L. 2008, MNRAS, 391, 481
Springel, V., Di Matteo, T., & Hernquist, L. 2005, ApJ, 620, L79
Taghizadeh-Popp, M., Kim, J. W., Lemson, G., et al. 2020, Astron. Comput., 33
Van Breugel, W., Filippenko, A., Heckman, T., & Miley, G. 1985, ApJ, 293, 83
Véron-Cetty, M.-P., & Véron, P. 2010, A&A, 518, A10
Wake, D. A., Bundy, K., Diamond-Stanic, A. M., et al. 2017, AJ, 154, 86
Westfall, K. B., Cappellari, M., Bershady, M. A., et al. 2019, AJ, 158, 231
Woo, J.-H., Bae, H.-J., Son, D., & Karouzos, M. 2016, ApJ, 817, 108
Wright, E. L. 2006, PASP, 118, 1711
Zinn, P.-C., Middelberg, E., Norris, R. P., & Dettmar, R.-J. 2013, ApJ, 774, 66